THE JOURNAL OF PHYSICAL CHEMISTRY C
A JOURNAL OF THE AMERICAN CHEMICAL SOCIETY

pubs.acs.org/JPCC

Article

Grain-Size-Governed Shear Failure Mechanism of Polycrystalline Methane Hydrates

Henrik Andersen Sveinsson,* Fulong Ning, Pinqiang Cao, Bin Fang, and Anders Malthe-Sørenssen

Cite This: *J. Phys. Chem. C* 2021, 125, 10034−10042

Read Online

ACCESS | Metrics & More | Article Recommendations | Supporting Information

ABSTRACT: The shear failure mechanism of polycrystalline gas hydrates is critical for understanding marine geohazards related to gas hydrates under a changing climate and for safe gas recovery from gas hydrate reservoirs. Since current experimental techniques cannot resolve the mechanism on a spatial and temporal nanoscale, molecular simulations can assist with proposing and substantiating nanoscale failure mechanisms. Here, we report the shear failure of polycrystalline methane hydrates using direct molecular dynamics simulations. Based on these simulations, we suggest two modes of shear behavior, depending on the grain sizes, d, in the polycrystal: grain-size-strengthening behavior with a $d^{1/3}$ grain size dependence for small grain sizes and grain-size-weakening behavior for large grain sizes. Through the crossover from strengthening to weakening behavior, the failure mode changes from shear failure with a failure plane parallel to the applied shear to tensile failure with a failure plane lying at an angle with the applied shear, spanning a network of grain boundaries. The existence of such a change in mechanism suggests that the Hall−Petch breakdown in methane hydrates is due to a change from grain boundary sliding to tensile opening being the most important failure mechanism when the grain size increases.

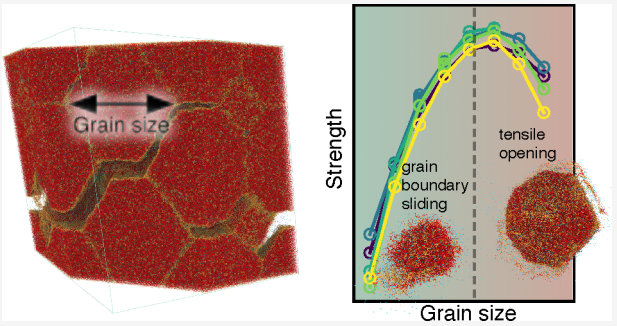

INTRODUCTION

Gas hydrates, also known as clathrate hydrates, are ice-like crystalline host−guest compounds. In gas hydrates, gas molecules—the guests—are encapsulated in a network formed by hydrogen-bonded water molecules forming a host lattice.[1] Gas hydrates normally form out of an aqueous solution of gas and water under high pressure and low temperatures. In nature, most gas hydrates are *methane* hydrates that are embedded in hydrate-bearing sediments. Such sediments are prevalent under the seabed on continental margins and under Arctic tundra, where a gas supply and suitable thermodynamic conditions are provided.[2] Gas hydrates can also form as plugs in oil production lines.[3] Over the last few decades, much attention has been directed toward hydrates as an energy resource[4,5] and their possible environmental impact.[6] Estimates of the global gas hydrate inventory vary by orders of magnitude, but a common and conservative estimate is approximately 1500 gigatons of carbon.[7] This estimate is an order of magnitude larger than current worldwide conventional natural gas reserves of approximately 120 gigatons of carbon (approximately 200 trillion m^3 STP[8]).

Gas hydrates may be distributed in various ways in a sedimentary matrix. These distribution patterns are commonly referred to as pore-filling, load-bearing, and cementing morphologies. In load-bearing and cementing morphologies, hydrates themselves make up an essential part of the overall stability of hydrate-bearing sediments.[9] Therefore, hydrates are important to the stability of marine slopes, Arctic subsea permafrost, and onshore permafrost. The stability of marine slopes and Arctic tundra relates to naturally occurring geohazards such as underwater landslides and explosive methane blow-outs from pingos in the Arctic,[10] which may lead to methane emissions that reach the atmosphere. The mechanical properties of hydrates are also important for risk assessment in subsea operations involving hydrates, both when drilling through hydrate-bearing sediments in conventional oil and gas recovery and when drilling *into* hydrate formations for the recovery of methane from the hydrate-bearing sediment itself.

The mechanical properties of gas hydrate-bearing sediments depend on the hydrate distribution pattern in the sediments, hydrate saturation, porosity, particle size, and mineral composition of the sediment skeleton.[9,11−18] Many studies have focused on the role of the hydrate distribution and content but not on the contribution of the mechanical behavior of the hydrate itself to that of sediments. Millimeter-scale observations of failure mechanisms for cemented hydrate-bearing sediments have shown that breakage

Received: January 31, 2021
Revised: March 27, 2021
Published: April 29, 2021

https://doi.org/10.1021/acs.jpcc.1c00901
J. Phys. Chem. C 2021, 125, 10034−10042

of the hydrate mass itself occurs during shearing,[17] and hydrate-bearing sediments tend to become both stronger and more brittle with increasing hydrate saturation.[19] Therefore, understanding the mechanical properties of the hydrate mass itself is fundamental to understanding the mechanical response of gas hydrate-bearing sediments.[20]

To date, only a small number of investigations on the mechanical behaviors of pure gas hydrates under tensile and compression conditions have been performed by laboratory measurements and molecular dynamics simulations. For example, it has been shown that laboratory-formed methane hydrate is 20- to 40-fold more creep resistant than ice (Ih) and experiences extensive strain hardening followed by strain softening.[21] Mechanical tests on massive natural gas hydrate samples have revealed brittle failure under reservoir conditions, with a strength of approximately 3 MPa. Molecular simulations have identified micromechanisms related to guest molecules,[22] shown some intrinsic differences between the failure of flawless single crystal samples of ice and hydrate,[23] and estimated the thermal activation of fracture initiation in monocrystalline methane hydrates.[24] Recently, the role of ice in the mechanical response of ice-containing methane hydrates was elaborated based on molecular simulations.[25]

Most gas hydrates, both in natural and laboratory settings, are grain-textured polycrystalline icy compounds,[26−28] and the grain size is important to the strength of polycrystalline materials. Grain sizes of laboratory-grown methane hydrates can be on the order of a micrometer or tens of micrometers, with very slow coarsening after initial formation of a polycrystal.[28] In nature, due to longer available coarsening times than in controlled experiments, the grain sizes can become hundreds of micrometers.[29] Molecular simulations have shown that grain size is a main factor controlling the mechanical behaviors of polycrystalline hydrates under tensile loading[30] and that the grain size dependence exhibits Hall−Petch behavior: the sample becomes weaker with increasing grain size above some critical grain size. The same study also showed a reverse Hall−Petch effect for small grain sizes, with a crossover at approximately 20 nm. However, most instabilities of gas hydrate-bearing sediments present as shear failures, and investigations on the deformation and failure mechanisms of polycrystalline gas hydrates under shear loading have not, to our knowledge, been performed before.

Here, we report the shear deformation and failure behaviors of polycrystalline methane hydrates with a range of grain sizes and the destabilization mechanisms elucidated by molecular dynamics simulations. We observe a Hall−Petch-like behavior similar to that for tensile failure,[30] but additionally, we observe a clear change in the failure mechanism with an increasing grain size of the polycrystal. For small grain sizes, the damage to the interior of grains is appreciable, and the failure plane is parallel to the applied shear. For larger grain sizes, the failure becomes fracture-like, the strength decreases, the fracture mode becomes tensile, and the failure plane becomes inclined with respect to the applied shear. We quantify this behavior and fit it to a model for the strength of small-grained solids.

Figure 1 shows an overview of this study, with the geological setting, the selection of a methane hydrate polycrystal as the focus of the preset study and the goal of discovering failure mechanisms and establishing mathematical models for the failure process.

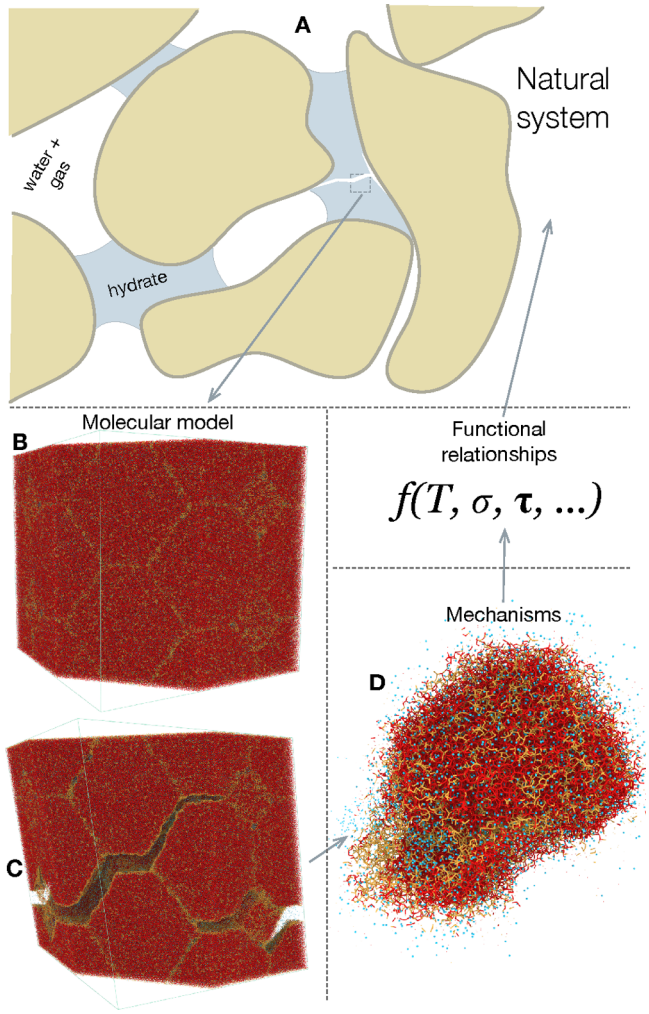

Figure 1. Conceptual view of this study. The motivation is to understand the mechanical behavior of gas hydrate-bearing sediments (A). In this study, we focus on the hydrate itself at the nanometer scale using molecular dynamics simulations. An example of a model system with a grain size of 24 nm is shown in panels B and C. We show both the initial, relaxed state and a strained, fractured state during a simulation. From these simulations, we identify failure mechanisms at the grain level (D) and find functional relationships that describe the behavior of hydrates as a function of conditions such as temperature T, axial stress σ, and shear stress τ. These may in turn be used to improve the description of gas hydrate-bearing sediments. Colors in the panels with molecular systems indicate whether molecules are hydrate sI coordinated (red) or not (orange). Methane molecules are blue. This coloring highlights the grain boundaries, where the accommodation of two different crystal directions along a plane results in a structure that is not perfectly sI.

SIMULATIONS

We performed multiple large molecular dynamics simulations of polycrystalline methane hydrates under shear loading. A molecular dynamics simulation is a solution of Newton's second equation for a system of many point particles. These particles act on each other with forces that represent, in an approximated way, the interactions between atoms and molecules.

Following Wu et al.,[30] we prepared cubic configurations of polycrystalline hydrates at full occupancy by the Voronoi tesselation of a BCC structure with 2 × 2 × 2 unit cell repetitions, resulting in 16 grains shaped like cube-truncated

https://doi.org/10.1021/acs.jpcc.1c00901
J. Phys. Chem. C 2021, 125, 10034−10042

octahedra. We created such systems with grain sizes ranging from 4 to 32 nm, corresponding to system sizes ranging from $(10\ \text{nm})^3$ (31 716 particles) to $(80\ \text{nm})^3$ (15 877 611 particles). Figure 1B shows snapshots from one of the simulations in the present study.

The methane hydrate was modeled using a monatomic water and methane model (mW).[31] This model has the same mathematical form as the Stillinger−Weber force field (see Computational Details). Monatomic water has been shown to reproduce the isotropicity, elastic modulus and Poisson's ratio of sI methane hydrate (Figure S2). The fracture toughness of monocrystalline sI hydrate using mW has been estimated to be 0.08 MPa$\sqrt{\text{m}}$,[24] which is close to the experimentally reported strengths of pure water ice[32,33] and only slightly higher than the fracture toughness of sI hydrate modeled with TIP4P/ice.[34] The monatomic water model allows for the growth of both amorphous and crystalline hydrates and can spontaneously produce hydrates where amorphous, sI and sII hydrates coexist.[35] Furthermore, it has been shown that the mW model presents similar mechanical response of polycrystalline hydrates as TIP4P/ice and TIP4P/2005.[30] Thus, it should be possible to discover mechanisms of hydrate failure in the emergent behavior of an mW methane hydrate.

Note, however, that monatomic water is coarse grained, and in particular, it uses a three-particle interaction between "water particles" to mimic the geometry and charge. There are several issues with the mW model that should be noted: The diffusivity of the liquid phase is far from experimental water, both in terms of the absolute value and the variation with changing temperature. The removal of explicit hydrogens prohibits proton disorder, so failure mechanisms depending crucially on proton disorder will not be present. Proton disorder has for example been shown crucial for achieving elastic anisotropy of hexagonal ice (Ih) in simulations.[36] Since sI hydrates are isotropic, this is less of a problem in the present study. Proton disorder should also influence the mobility of grain boundaries, since the number of possible grain boundary configurations necessarily must increase. Monatomic water also enforces tetrahedral order rather than letting it arise spontaneously from the shape and charge distribution of the water molecule. This prohibits, for instance, the formation of high-density liquid water at extreme pressures (0.7 GPa).[37] This is, however, far beyond the pressures we apply in this study. The choice of the mW water model in this study is grounded in its superior computational performance, good elastic properties and tensile fracture strength values for sI hydrate in addition to its ability to spontaneously growing several different hydrate phases.

We subjected the polycrystals in the simulations to simple shear at a constant rate of $2.5 \times 10^7\ \text{s}^{-1}$ and a normal pressure of 10 MPa, corresponding approximately to a 1 km water column. These simulations were performed for different temperatures ranging from 263.15 to 288.15 K, spanning the relevant temperature range for hydrates in nature. All simulations were run long enough for the methane hydrate polycrystals to fail mechanically, allowing us to measure a maximum shear stress and to assess the residual strength. We produced four replicate simulations with different initial velocity seeds for two of the temperature−grain size combinations, (273.15 K, 11.9 nm) and (283.15 K, 15.9 nm), to estimate the variation in the maximum stress due to chance. An example snapshot of a system during mechanical failure is shown in Figure 1C. A high strain rate was necessary to keep the computational cost of running the molecular dynamics simulations at an acceptable level. Note that if we translate these high strain rates into shear speeds, they are not unreasonably high. A representative simulation with a box height of 40 nm has a shear speed of 1 m/s, which is a reasonable real-world sliding velocity. Thus, a high strain rate can be warranted if the goal of the simulations is to discover mechanisms at play close to a failing interface, where deformation rates are higher than the global steady-state creep rate of the experiments.

COMPUTATIONAL DETAILS

Calculation of Grain Boundary Traction. The main facets of the grains in our model polycrystal have a normal vector $\mathbf{n} = (\pm1, \pm1, \pm1)$. Each such grain boundary is associated with a hexagonal face of two neighbor grains in the polycrystal. Therefore, we consider the grain boundary region to be the hexagonal prism centered on the grain boundary and with a height of 1 nm. We take the average virial stress, S, including the velocity contribution, over this volume. We average over 1000 consecutive time steps = 10 ps. The virial stress has been shown to resolve the local stress field under mechanical loading of solid molecular systems, even under conditions of dynamic fracture.[38]

For each particle, i, the virial stress is taken over neighboring particles j as

$$\sigma^i_{\alpha\beta} = -mv_\alpha v_\beta + \frac{1}{2}\sum_j (r^i_\alpha - r^j_\alpha)F^{ij,\text{pair}}_\beta \tag{1}$$

$$+ \frac{1}{3}\sum_{j,k} r^i_\alpha F^{ijk,\text{three}}_\beta + r^j_\alpha F^{jki,\text{three}}_\beta + r^k_\alpha F^{kij,\text{three}}_\beta \tag{2}$$

where α and β denote the components of the stress tensor (e.g., σ_{xx} or σ_{xz}). The first sum is over forces from pair interactions with particle i and neighbors j within the cutoff distance r_c, and the second sum is over forces from three-body interactions. The notation r^i_α means the α component of the position vector of particle i. $F^{ij,\text{pair}}_\beta$ is the β component of the two-body force acting on particle i due to particle j. $F^{ijk,\text{three}}_\beta$ is the three-body force acting on particle i due to particles j and particle k. We rotate the stress tensor so as to find the normal and shear traction on all of the $(\pm1, \pm1, \pm1)$ grain boundaries. We only use the local stress calculation to compute the ratio of normal to shear traction, the ratio of maximum shear and maximum normal stress and to illustrate the sign of the normal stress on particular grain boundaries. This means that we do not need to compute the atomic volume, which we would have had to do if we were after the actual values of the local stress.

The $(\pm1, \pm1, \pm1)$ grain boundaries geometrically group into two kinds within which the boundaries are geometrically equivalent with respect to xz shear. The difference between these are whether they experience tension or compression, as illustrated in Figure 4, parts E and F. Therefore, we take the average of the magnitude of the normal and shear traction, separately, for each type of grain boundary.

Preparation of Polycrystals. We used literature values[39] for the oxygen and hydrogens in the unit cell of sI methane hydrate. Since we use the mW model, this is not strictly necessary, and we could have just taken the idealized space group description along with the oxygen and methane positions of the primitive cell.

https://doi.org/10.1021/acs.jpcc.1c00901
J. Phys. Chem. C 2021, 125, 10034−10042

The polycrystals were created like in ref 30: First, we generate a (2 × 2 × 2) periodic body-centered cubic (BCC) structure. This structure is used as the sites in a three-dimensional Voronoi diagram. Since the (2 × 2 × 2) BCC structure contains 16 points, this procedure results in 16 Voronoi cells, each of which define the extent of a randomly oriented single crystal of structure I methane hydrate in our polycrystal.

Force Fields. Methane and water molecules were described as one particle per molecule using the monatomic water and methane model (mW) by Jacobson and Molinero.[31] The potential function of this force field is the same as that for the Stillinger−Weber force field:

$$U = \sum_i \sum_{j>i} \phi_2(r_{ij}) + \sum_i \sum_{j\neq i} \sum_{k>j} \phi_3(r_{ij}, r_{ik}, \theta_{ijk})$$

$$\phi_2(r_{ij}) = A_{ij}\varepsilon_{ij}\left[B_{ij}\left(\frac{\sigma_{ij}}{r_{ij}}\right)^{p_{ij}} - \left(\frac{\sigma_{ij}}{r_{ij}}\right)^{q_{ij}}\right] \exp\left(\frac{\sigma_{ij}}{r_{ij} - a_{ij}\sigma_{ij}}\right),$$

$$\phi_3(r_{ij}, r_{ik}, \theta_{ijk}) = \lambda_{ijk}\varepsilon_{ijk}[\cos\theta_{ijk} - \cos\theta_{0ijk}]^2 \exp\left(\frac{\gamma_{ij}\sigma_{ij}}{r_{ij} - a_{ij}\sigma_{ij}}\right) \exp\left(\frac{\gamma_{ik}\sigma_{ik}}{r_{ik} - a_{ik}\sigma_{ik}}\right) \quad (3)$$

with a cutoff distance for interactions at $r_c = a\sigma$, where both the potential function and the forces vanish smoothly.

The mW force field is about 2 orders of magnitude more efficient in terms of simulated mass × time per CPU-hour than the all-atom TIPnP potentials. The parameters of this potential are given in Table 1.

Simulation Setup. All simulations were performed in Lammps.[40] A Nosé−Hoover thermo-baro-couple[41] with damping coefficients of T_{press} = 1 ps and T_{temp} = 0.2 ps was used to mimic *NPT* conditions. The equations of motion were integrated using the Velocity Verlet scheme with a time-step of 10 fs. The polycrystals were first allowed to anneal for 10 ns at T = 283.15 K and P = 10 MPa in order for the grain boundaries to relax. After annealing, shear strain was applied at a rate of 2.5 × 10^7 s^{-1} by shearing the simulation domain. Shear was applied for long enough for the system to fail mechanically. During shearing, the thermo-baro-couple was $NP_xP_yP_z(xy)(xz)(yz)T$, with xz being the applied shear and xy and yz being kept constant at 0. This means that we used a modified *NPT* ensemble with a constant anisotropic pressure in the lateral directions, while the shear directions were under strain control, with xy = 0, yz = 0, and xz being dictated by the applied strain rate.

Table 1. Values of Parameters in the Monatomic Water and Methane Potential by Jacobson and Molinero[31]

common parameters[a]	
A	7.049 556 277
B	0.602 224 558 4
γ	1.2
a	1.8
θ_0	109.5°
water−water	
ε_{ww}	6.189 kcal/mol
σ_{ww}	2.3925 Å
λ_{www}	23.15
methane−methane	
ε_{mm}	0.340 kcal/mol
σ_{mm}	4.08 Å
λ_{mmm}	0
water−methane interactions	
ε_{wm}	0.180 kcal/mol
σ_{wm}	4.00 Å
$\lambda_{wm(mlx)}$	0

[a]Same as in the original Stillinger−Weber potential.

RESULTS

The behavior of the polycrystal depends strongly on the grain size. Figure 2A shows the stress−strain relationships for simulations at a range of grain sizes and T = 273.15 K. For the

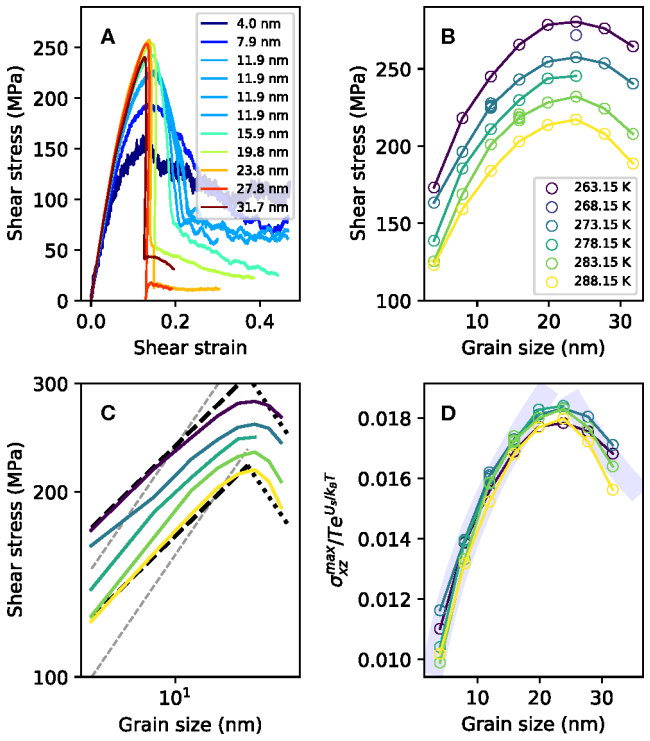

Figure 2. Shear strength of polycrystalline methane hydrates. (A) shows loading curves for T = 273.15 K. The legend shows the grain size, d, calculated from the grain volume: $d = V^{1/3}$. (B) Strength of hydrate samples as a function of the grain size for different temperatures. (C) Data from part B with a logarithmic scale on both axes, with lines corresponding to grain size dependence exponents of $^1/_3$ (dashed black lines) and $-^1/_2$ (dotted black lines). A $^1/_2$ power law is also indicated (dashed gray lines) to contrast the $^1/_3$ power law. (D) Data from part B on axes that should reveal the grain size dependence of the shear strength given that eq 4 describes the temperature dependence of the shear strength correctly. Grain size dependence exponents of $^1/_3$ and $-^1/_2$ are indicated with thick gray lines in the small grain size and large grain size parts of panel D, respectively. Notice that for two of the temperature−grain size combinations, (273.15 K, 11.9 nm) and (283.15 K, 15.9 nm), four simulations with different random initial velocity seed have been run to show that the variance of the maximum stress is very small compared to the difference between the temperature groups. These show up as mostly overlapping markers in panel B, and as several loading curves with the same grain size in panel A.

https://doi.org/10.1021/acs.jpcc.1c00901
J. Phys. Chem. C 2021, 125, 10034−10042

smallest grain size, 4 nm, the hydrate shows ductile characteristics with a relatively low maximum strength. The loading curve starts elastically at low strains before reaching an initial yield stress of approximately 120 MPa at a strain of approximately 0.08. The hydrate then hardens before it reaches its ultimate yield stress of approximately 150 MPa. Then, strain softening follows but not catastrophic failure. Increasing the grain size leads to a shorter hardening phase, a more abrupt failure process and a smaller residual strength—the hydrate behaves in more brittle fashion. For grain sizes from 19.8 nm and up, the failure is more or less instant. We also see that the markers for the data points with replicates, (273.15 K, 11.9 nm) and (283.15 K, 15.9 nm), fall almost on top of each other, showing that the variance is much smaller than the difference between the temperature groups.

To assess the effect of the grain size and temperature simultaneously, we estimate the shear strength by taking the maximum of the stress−strain relationship from each simulation. Figure 2B shows the maximum shear stress as a function of grain size for different temperatures. It shows grain size strengthening for small grain sizes, up to a critical grain size of $d \approx 22$ nm, and grain size weakening for larger grain sizes. Increasing temperatures lead to a decreasing strength. Figure 2C shows the same data with a logarithmic scale on both axes to reveal power-law relationships. We find that an exponent of approximately $^1/_3$ fits well in the grain size strengthening regime. We do not have enough data in the larger grain size limit to make any strong conclusions, but we draw a $1/\sqrt{d}$ relationship for reference. Beyond the critical grain size, the slopes of the maximum stress−grain size relationships seem to vary systematically: they are steeper for higher temperatures.

We expect that the temperature dependence of the strength can be explained by an energy activation model. Such an approach has worked previously to describe tensile cracks in hydrates by molecular dynamics simulations.[24] Following a study on nanocrystalline metals,[42] we assume a grain sliding model for the strength:

$$\sigma_{\max} = A(d)\dot{\varepsilon}Te^{U_s/k_BT} \tag{4}$$

Here $A(d)$ captures the grain size dependence, $\dot{\varepsilon}$ is the strain rate, T is the temperature, k_B is the Boltzmann constant, and U_s is an energy barrier to grain boundary sliding. We therefore seek to collapse all the maximum stresses measured in our simulations onto a common scaling function $A(d)$ by dividing them with Te^{U_s/k_BT} for some activation energy U_s. Since this activation model was developed for the nanocrystalline branch, we prioritize the data points below the critical grain size in the model fit. We obtain the data collapse shown in Figure 2D by setting $U_s = 0.095$ eV. This data collapse shows that the data fit the proposed model well below the critical grain size and slightly less accurately for grain sizes beyond the critical grain size of $d \approx 22$ nm. In addition to the collapsed data points, we draw eye-guiding lines corresponding to a $d^{1/3}$ grain size dependence below the critical grain size and $d^{-1/2}$ beyond the critical grain size.

More than just showing the behavior, molecular dynamics simulations allow for direct observation of which mechanisms change during a change in behavior. We find that the grain size strengthening to weakening behavior is accompanied by a change in the failure mechanism that is both visually striking and numerically measurable. Figure 3 shows grains of different

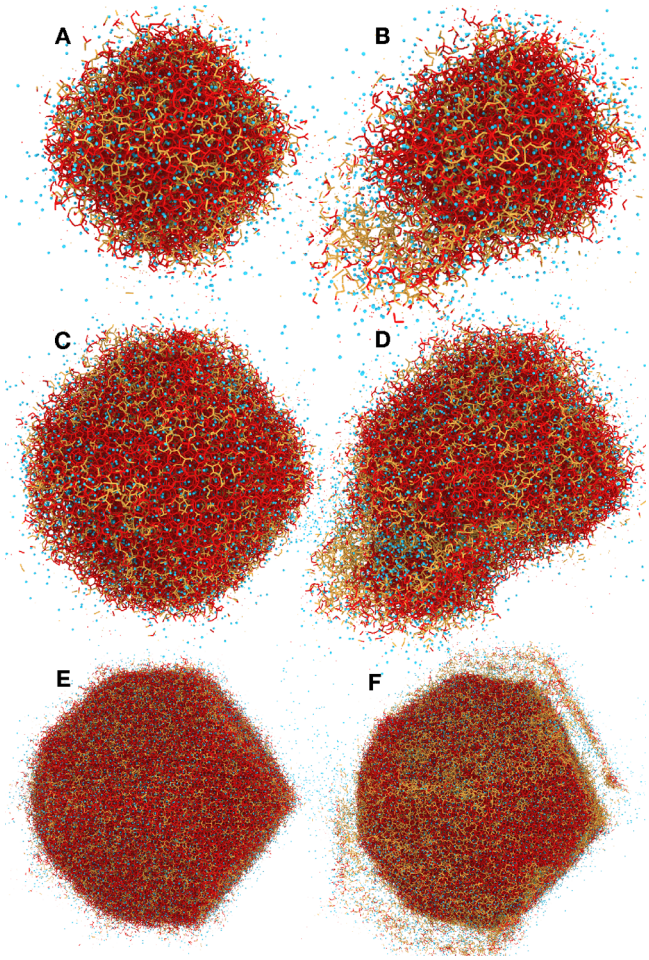

Figure 3. Damage pattern changes from grain interior damage for small grain sizes to grain boundary opening for larger grains. This is illustrated by single grains taken out from simulations with grain sizes of 8 nm (A, B), 12 nm (C, D), and 24 nm (E,F) and $T = 273.15$ K. The colors show whether particles are sI coordinated hydrate (red), non sI coordinated hydrate (orange) or methane (blue) and thus visualize damage to the grains and in particular show the grain boundary. Panels B and D show that for small grain sizes, the interior of grains is damaged, while panel F shows that the damage pattern for larger grains boundaries is tensile opening.

sizes just after failure of the sample. For small grains, at 8 nm, it seems that grain corners are worn off. For slightly larger grains, at 12 nm, we observe intragrain fracture, resulting in parts of certain grains being torn off. When intragrain fractures occur, they are accompanied by the formation of a methane bubble. For grains at 8 and 12 nm, the overall failure plane in the whole system is parallel to the applied shear. However, for larger grains, especially for $d \geq 19.8$ nm, the failure mechanism changes completely. Failure now occurs exclusively at the grain boundaries by the opening of cavities. The failure appears as a tensile fracture of the boundaries, resulting in a failure plane that lies on a slope with respect to the applied shear and spanning a network of grain boundaries (see also Figure S1).

To verify quantitatively that the failure mode changes from shear failure to tensile failure, we check how the normal and shear traction on the grain boundaries change with grain size and temperature. The grains resulting from Voronoi tesselation of a body-centered cubic structure mainly have grain boundaries with normal vectors in the $(\pm1, \pm1, \pm1)$

https://doi.org/10.1021/acs.jpcc.1c00901
J. Phys. Chem. C 2021, 125, 10034−10042

coordinate directions. These grain boundaries have two features with respect to the applied shear: those under tension and those under compression, since one of the *xz*-plane diagonals contracts and the other expands under *xz* shear. The stresses on the two kinds of grain boundaries are shown in Figure 4, parts E and F. We find a normal and shear traction, σ_n and τ_n, respectively, on these surfaces. These traction components should act toward a perfectly tensile (σ_n) or perfectly shear (τ_n) failure of the grain boundary. The ratio of the normal to shear traction is shown in Figure 4, parts A and B. In addition, parts C and D of Figure 4 show the ratio of the maximum normal to maximum shear stress as calculated from the principal stresses. The absolute value of the ratio σ_n/τ_n increases and then stabilizes with grain size, but the value where it stabilizes depends on the temperature for both the tensile and compressive boundaries.

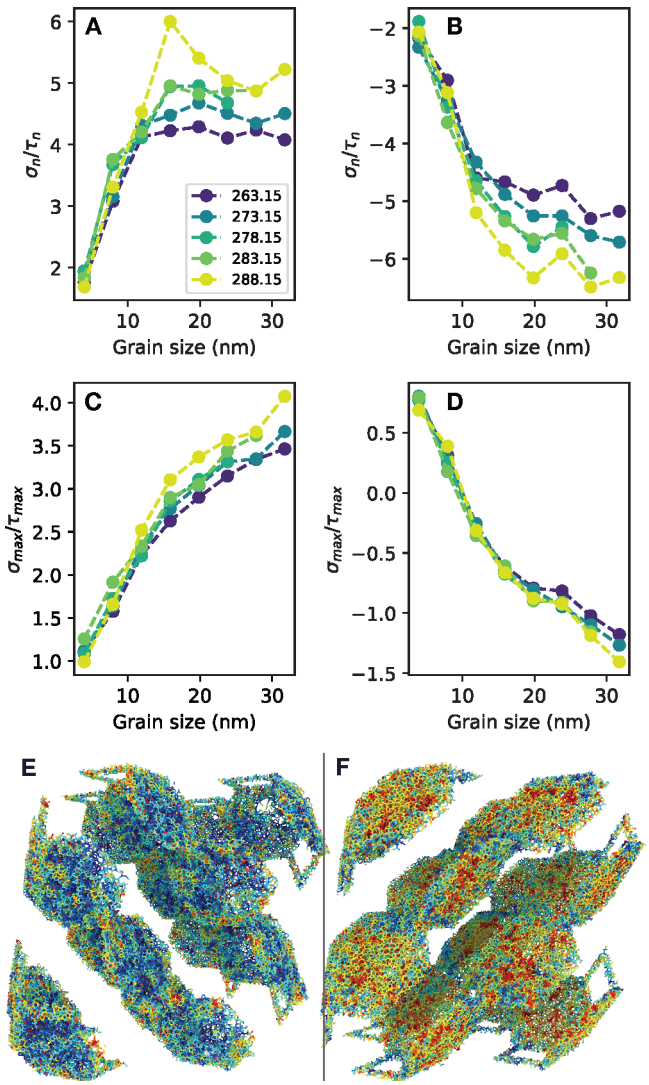

Figure 4. Ratio of normal to shear traction on (111) grain boundaries under tension (A, C) and compression (B, D) as a function of grain size for different temperatures. The relative normal traction increases drastically with grain size, indicating a change in the failure mode. Panels E and F illustrate the parts of the system over which the traction is calculated (see methods section for details on the calculation). The colors in parts E and F indicate local stress from blue (tension) to red (compression).

DISCUSSION

We have shown that the shear failure of polycrystalline methane hydrates follows a reverse Hall−Petch relationship up to a critical grain size of $d \approx 22$ nm and a regular Hall−Petch relationship beyond this critical grain size. The crossover between these Hall−Petch regimes is accompanied by a pronounced change in the failure mode; it changes from shear to tensile. We also find that the temperature dependence below the critical grain size fits with an activation energy of 0.095 eV. This activation energy does not capture the temperature variation to the same extent beyond the critical grain size. This is consistent with a change in mechanism. We have not found experimentally measured activation energies for nanocrystalline methane hydrates, so we settle on comparing them with nanocrystalline metals: In molecular dynamics simulations of nanocrystalline Ni at temperatures from 300 to 500 K, an activation energy of 0.2 eV has been measured.[43] This is higher than in the present study, which is expected for a stronger material with a higher melting point. The melting point of Ni is 1728 K, its Young's modulus is around 200 GPa, and its fracture toughness is on the order of 50 MPam$^{1/2}$. Compare to values of around 290 K, 7 GPa, and 0.1 MPam$^{1/2}$ for sI hydrate.

The failure is brittle above the critical grain size. Consequently, shear failures of hydrate polycrystals in experiments, whose grain sizes are far larger than those in our simulations, should be brittle. This is compatible with experimental observations, suggesting that hydrate-bearing sands become increasingly brittle with increasing hydrate saturation[19] and that crushing of the hydrate mass itself is important during the failure of hydrate-bearing sands.[17,44] This is also consistent with experiments on massive natural gas hydrates showing brittle behavior.[45] In the experiment on massive hydrates, they also constructed a range of failure stresses as a function of grain size based on their experiments, previous molecular simulations, and previous experiments on ice. Our simulations from the grain-size weakening regime all fall inside this range, increasing our confidence in the quantitative accuracy of our results. We expect that decreasing the strain rate will, to a first order approximation, reduce the maximum stresses in our simulations. A second order effect of this is presumably that the brittle mechanism for large grain sizes is impeded more than the ductile mechanism at small grain sizes. Thus, for a lower strain rate, we would expect the crossover length, d_m, to increase.

The computational cost of increasing the system size is considerable since the number of atoms increases 8-fold for each doubling of the grain size d. We have established that the interior of grains stays intact during the failure of large grains. Therefore, rather than just scaling up the simulations of the present study, multiscale approaches using explicit molecules only on grain boundaries and grain junctions can be a way to reveal the mechanisms on larger scales and to accurately determine whether an energy activation model, and if so what activation energy, holds above the critical grain size. This activation model could, for instance, be of a similar nature to that for slow tensile crack evolution in monocrystalline hydrates.[24] In that model, for penny-shaped cracks with a length of 8 nm, an activation energy on the same order as measured in the present study (0.095 eV) could be achieved by setting the maximum stress to approximately 560 MPa, and

https://doi.org/10.1021/acs.jpcc.1c00901
J. Phys. Chem. C 2021, 125, 10034−10042

lowering the maximum stress would increase the activation energy.

The possible number of polycrystal configurations is vast, both in terms of the rotations and geometries of the crystal grains constituting the polycrystal. The polycrystals in the present study represents an idealized case. Previous studies[30,46] have shown that polycrystals with uniformly randomly Voronoi-centered grains, present similar *tensile* behavior as their regularly constructed (BCC structure) counterparts. We may therefore reasonably conjecture that the effects observed in the present study will hold for more disorderly polycrystals.

The grain size dependence revealed in this study is similar to that observed under tension and compression.[30] However, under shear loading, we find that the change in the failure mechanism as the grain size crosses the critical grain size is much more pronounced. There is a clear change from failure that tears off parts of hydrate grains to failure that only involves grain boundary opening. During this change, we can measure that the tensile proportion of the grain boundary traction increases and that it stabilizes with grain size on a temperature-dependent value. We are not comfortable estimating the activation energy during tensile opening because the data beyond the crossover length are sparse. However, the order of the data points in the data collapse (Figure 2D) shows that the high-temperature data points still lie below the low-temperature data points after applying scaling axes. We can therefore with reasonable certainty state that this activation energy would have to be larger than the activation energy controlling the small-grained regime.

Grain size weakening in polycrystalline materials is often explained by the Hall−Petch effect. In the Hall−Petch effect, dislocations pile up at the grain boundary, resulting in the yield strength following a $1/\sqrt{d}$ dependence, where d is the grain size. When the grain size d is very small, on the order of a few crystal unit cells, the polycrystal commonly strengthens with grain size. However, in our simulations, we do not find dislocations piling up prior to failure. Rather, all damage is concentrated on the grain boundaries and junctions, and only at critical failure do some grains in the small-grain regime experience interior damage. Mechanisms other than dislocation pile-up have been proposed to explain grain size weakening and strengthening in nonmetals, such as ceramics,[47] where a critical grain size of 18.4 nm is found, which is explained by the relative fractions of bulk, grain boundary, and triple junction volume in a polycrystal. In that study, such an analysis was consistent with a grain size dependence d^{η} with the exponent η being smaller than $^1/_2$ below the critical grain size.

A polycrystal can absorb simple shear in various ways. If we assume that the grain boundary sliding is insensitive to normal traction and is corrected for the confining pressure, the compressive normal traction on the (111) grain boundaries under compression would be equal to the tensile normal traction on the (111) grain boundaries under tension. Conversely, if the grain boundary sliding depended on normal traction, the compressive boundaries would have a different ratio of shear to normal traction due to preserving shear traction in the absence of grain boundary sliding. The symmetric and grain-size increasing tendency shown in Figure 4, parts A and B, indicates that the tension and compression built up from grain boundary sliding plays an increasingly important role as the grain size increases, that grain boundary sliding is largely insensitive to normal traction, and that temperature effects interact with the grain size. Future studies could therefore benefit from systematically examining the sliding properties of various hydrate grain boundary configurations.

The measured grain sizes in real hydrates are larger than those we modeled in this study. However, smaller grains may form during failure. For instance, during laboratory-controlled failure of old Antarctic water ice, small, recrystallized ice grains of approximately 100 μm formed in the grain boundaries between the original millimeter-sized grains.[48] If a similar mechanism exists for hydrates, the slow coarsening of hydrates[28] could possibly lead to a strong small-grained boundary zone facilitating high creep resistance.

CONCLUSIONS

Understanding the failure mechanisms of polycrystalline methane hydrates is important for predicting the behavior of gas hydrate-bearing sediments. In this paper, we have shown simulations suggesting that the mechanism of shear failure of polycrystalline methane hydrates is grain-size dependent, with a transition from local shear failure to local tensile failure with increasing grain size. This change in mechanism coincides with a crossover from grain size strengthening to grain size weakening behavior, indicating that a change from local shear to local tensile failure is responsible for the Hall−Petch breakdown in polycrystalline methane hydrates.

ASSOCIATED CONTENT

Supporting Information

The Supporting Information is available free of charge at https://pubs.acs.org/doi/10.1021/acs.jpcc.1c00901.

Illustration of the change of mechanism of failure when the grain size increases and Young's modulus and Poisson's ratio as a function of temperature for the force field used in the present study (PDF)

AUTHOR INFORMATION

Corresponding Author

Henrik Andersen Sveinsson − *The NJORD Centre, Department of Physics, University of Oslo, 0371 Oslo, Norway*; orcid.org/0000-0002-3651-0710; Email: h.a.sveinsson@fys.uio.no

Authors

Fulong Ning − *Faculty of Engineering, China University of Geosciences, Wuhan, Hubei 430074, China; Laboratory for Marine Mineral Resources, Qingdao National Laboratory for Marine Science and Technology, Qingdao 266237, China*; orcid.org/0000-0003-1236-586X

Pinqiang Cao − *Faculty of Engineering, China University of Geosciences, Wuhan, Hubei 430074, China; School of Resource and Environmental Engineering, Wuhan University of Science and Technology, Wuhan, Hubei 430081, China*; orcid.org/0000-0003-1469-4288

Bin Fang − *Faculty of Engineering, China University of Geosciences, Wuhan, Hubei 430074, China*

Anders Malthe-Sørenssen − *The NJORD Centre, Department of Physics, University of Oslo, 0371 Oslo, Norway*

Complete contact information is available at: https://pubs.acs.org/10.1021/acs.jpcc.1c00901

Notes

The authors declare no competing financial interest.

■ ACKNOWLEDGMENTS

H.A.S and A.M.-S. acknowledge support from the Research Council of Norway, FRINATEK Grant Number 231621. P.C., B.F. and F.N. acknowledge support from the National Key Research and Development Program of China (2018YFE0126400) and the Department of Natural Resources of Guangdong Province Project (GDNRC[2020]-047).

■ REFERENCES

(1) Sloan, E. D. Fundamental Principles and Applications of Natural Gas Hydrates. *Nature* **2003**, *426*, 353−359.
(2) Kvenvolden, K. A. Gas Hydrates−Geological Perspective and Global Change. *Rev. Geophys.* **1993**, *31*, 173−187.
(3) Hammerschmidt, E. Formation of Gas Hydrates in Natural Gas Transmission Lines. *Ind. Eng. Chem.* **1934**, *26*, 851−855.
(4) Boswell, R. Is Gas Hydrate Energy Within Reach? *Science* **2009**, *325*, 957−958.
(5) Moridis, G.; Collett, T.; Pooladi-Darvish, M.; Hancock, S.; Santamarina, C.; Boswell, R.; Kneafsey, T.; Rutqvist, J.; Kowalsky, M.; Reagan, M.; et al. Challenges, Uncertainties, and Issues Facing Gas Production From Gas-Hydrate Deposits. *SPE Reservoir Eval. Eng.* **2011**, *14*, 76−112.
(6) Phrampus, B. J.; Hornbach, M. J. Recent Changes to the Gulf Stream Causing Widespread Gas Hydrate Destabilization. *Nature* **2012**, *490*, 527−530.
(7) Boswell, R.; Collett, T. S. Current Perspectives on Gas Hydrate Resources. *Energy Environ. Sci.* **2011**, *4*, 1206−1215.
(8) Central Intelligence Agency *Natural Gas - Proved Reserves*; 2016.
(9) Waite, W.; Santamarina, J.; Cortes, D.; Dugan, B.; Espinoza, D.; Germaine, J.; Jang, J.; Jung, J.; Kneafsey, T.; Shin, H.; et al. Physical Properties of Hydrate-Bearing Sediments. *Rev. Geophys.* **2009**, *47*, RG4003.
(10) Andreassen, K.; Hubbard, A.; Winsborrow, M.; Patton, H.; Vadakkepuliyambatta, S.; Plaza-Faverola, A.; Gudlaugsson, E.; Serov, P.; Deryabin, A.; Mattingsdal, R.; et al. Massive Blow-Out Craters Formed by Hydrate-Controlled Methane Expulsion From the Arctic seafloor. *Science* **2017**, *356*, 948−953.
(11) Hyodo, M.; Li, Y.; Yoneda, J.; Nakata, Y.; Yoshimoto, N.; Nishimura, A.; Song, Y. Mechanical Behavior of Gas-Saturated Methane Hydrate-Bearing Sediments. *J. Geophys. Res. Solid Earth* **2013**, *118*, 5185−5194.
(12) Winters, W.; Waite, W.; Mason, D.; Gilbert, L.; Pecher, I. Methane Gas Hydrate Effect on Sediment Acoustic and Strength Properties. *J. Pet. Sci. Eng.* **2007**, *56*, 127−135.
(13) Yun, T.; Santamarina, J.; Ruppel, C. Mechanical Properties of Sand, Silt, and Clay Containing Tetrahydrofuran Hydrate. *J. Geophys. Res.* **2007**, *112*, B04106.
(14) Miyazaki, K.; Masui, A.; Aoki, K.; Sakamoto, Y.; Yamaguchi, T.; Okubo, S. Strain-rate Dependence of Triaxial Compressive Strength of Artificial Methane-Hydrate-Bearing Sediment. *Int. J. Offshore Polar Eng.* **2010**, *20*, 256−264.
(15) Priest, J. A.; Clayton, C. R.; Rees, E. V. Potential Impact of Gas Hydrate and its Dissociation on the Strength of Host Sediment in the Krishna−Godavari Basin. *Mar. Pet. Geol.* **2014**, *58*, 187−198.
(16) Pinkert, S.; Grozic, J. Prediction of the Mechanical Response of Hydrate-Bearing Sands. *J. Geophys. Res. Solid Earth* **2014**, *119*, 4695−4707.
(17) Yoneda, J.; Jin, Y.; Katagiri, J.; Tenma, N. Strengthening Mechanism of Cemented Hydrate-Bearing Sand at Microscales. *Geophys. Res. Lett.* **2016**, *43*, 7442−7450.
(18) Liu, Z.; Wei, H.; Peng, L.; Wei, C.; Ning, F. An Easy and Efficient Way to Evaluate Mechanical Properties of Gas Hydrate-Bearing Sediments: The Direct Shear Test. *J. Pet. Sci. Eng.* **2017**, *149*, 56−64.
(19) Liu, Z.; Dai, S.; Ning, F.; Peng, L.; Wei, H.; Wei, C. Strength Estimation for Hydrate-Bearing Sediments From Direct Shear Tests of Hydrate-Bearing Sand and Silt. *Geophys. Res. Lett.* **2018**, *45*, 715−723.
(20) Ning, F.; Yu, Y.; Kjelstrup, S.; Vlugt, T. J.; Glavatskiy, K. Mechanical Properties of Clathrate Hydrates: Status and Perspectives. *Energy Environ. Sci.* **2012**, *5*, 6779.
(21) Durham, W. B.; Kirby, S. H.; Stern, L. A.; Zhang, W. The Strength and Rheology of Methane Clathrate Hydrate. *J. Geophys. Res.* **2003**, *108*, 2182.
(22) Shi, Q.; Cao, P.; Han, Z.; Ning, F.; Gong, H.; Xin, Y.; Zhang, Z.; Wu, J. Role of Guest Molecules in the Mechanical Properties of Clathrate Hydrates. *Cryst. Growth Des.* **2018**, *18*, 6729−6741.
(23) Cao, P.; Wu, J.; Zhang, Z.; Fang, B.; Ning, F. Mechanical Properties of Methane Hydrate: Intrinsic Differences from Ice. *J. Phys. Chem. C* **2018**, *122*, 29081−29093.
(24) Sveinsson, H. A.; Malthe-Sørenssen, A. Molecular-Scale Thermally Activated Fractures in Methane Hydrates: A Molecular Dynamics Study. *Phys. Chem. Chem. Phys.* **2019**, *21*, 13539−13544.
(25) Cao, P.; Ning, F.; Wu, J.; Cao, B.; Li, T.; Sveinsson, H. A.; Liu, Z.; Vlugt, T. J.; Hyodo, M. Mechanical Response of Nanocrystalline Ice-Contained Methane Hydrates: Key Role of Water Ice. *ACS Appl. Mater. Interfaces* **2020**, *12*, 14016−14028.
(26) Stern, L.; Kirby, S. Natural Gas Hydrate in Sediments Imaged by Cryogenic SEM: Insights from Lab Experiments on Synthetic Hydrates as Interpretive Guides. *AGU Fall Meeting Abstracts* **2006**, OS33B1699.
(27) Stern, L. A.; Lorenson, T. D. Grain-scale Imaging and Compositional Characterization of Cryo-Preserved India NGHP 01 Gas-Hydrate-Bearing Cores. *Mar. Pet. Geol.* **2014**, *58*, 206−222.
(28) Chaouachi, M.; Neher, S. H.; Falenty, A.; Kuhs, W. F. Time Resolved Coarsening of Clathrate Crystals: The Case of Gas Hydrates. *Cryst. Growth Des.* **2017**, *17*, 2458−2472.
(29) Klapp, S.; Klein, H.; Kuhs, W. First Determination of Gas Hydrate Crystallite Size Distributions Using High-Energy Synchrotron Radiation. *Geophys. Res. Lett.* **2007**, *34*, L13608.
(30) Wu, J.; Ning, F.; Trinh, T. T.; Kjelstrup, S.; Vlugt, T. J.; He, J.; Skallerud, B. H.; Zhang, Z. Mechanical Instability of Monocrystalline and Polycrystalline Methane Hydrates. *Nat. Commun.* **2015**, *6*, 8743.
(31) Jacobson, L. C.; Molinero, V. A Methane−Water Model for Coarse-Grained Simulations of Solutions and Clathrate Hydrates. *J. Phys. Chem. B* **2010**, *114*, 7302−7311.
(32) Liu, H.; Miller, K. Fracture Toughness of Fresh-Water Ice. *J. Glaciol.* **1979**, *22*, 135−143.
(33) Benham, P. P.; Crawford, R. J.; Armstrong, C. G. *Mechanics of engineering materials*; Prentice Hall: 1996.
(34) Sveinsson, H. A. *Molecular Modeling of Fracture in Methane Hydrates*. M.Sc. Thesis; University of Oslo: 2015.
(35) Jacobson, L. C.; Molinero, V. Can Amorphous Nuclei Grow Crystalline Clathrates? The Size and Crystallinity of Critical Clathrate Nuclei. *J. Am. Chem. Soc.* **2011**, *133*, 6458−6463.
(36) Gudkovskikh, S. V.; Kirov, M. V. Proton Disorder and Elasticity of Hexagonal Ice and Gas Hydrates. *J. Mol. Model.* **2019**, *25*, 32.
(37) Guo, Q.; Ghaani, M. R.; Nandi, P. K.; English, N. J. Pressure-Induced Densification of Ice Ih under Triaxial Mechanical Compression: Dissociation versus Retention of Crystallinity for Intermediate States in Atomistic and Coarse-Grained Water Models. *J. Phys. Chem. Lett.* **2018**, *9*, 5267−5274.
(38) Buehler, M. J. *Atomistic Modeling of Materials Failure*; Springer: Boston, MA, 2008.
(39) Takeuchi, F.; Hiratsuka, M.; Ohmura, R.; Alavi, S.; Sum, A. K.; Yasuoka, K. Water Proton Configurations in Structures I, II, and H Clathrate Hydrate Unit Cells. *J. Chem. Phys.* **2013**, *138*, 124504.
(40) Plimpton, S. Fast Parallel Algorithms for Short-Range Molecular Dynamics. *J. Comput. Phys.* **1995**, *117*, 1−19.
(41) Shinoda, W.; Shiga, M.; Mikami, M. Rapid Estimation of Elastic Constants by Molecular Dynamics Simulation Under Constant Stress. *Phys. Rev. B: Condens. Matter Mater. Phys.* **2004**, *69*, 16−18.

https://doi.org/10.1021/acs.jpcc.1c00901
J. Phys. Chem. C 2021, 125, 10034−10042

(42) Borodin, E.; Mayer, A. A Simple Mechanical Model for Grain Boundary Sliding in Nanocrystalline Metals. *Mater. Sci. Eng., A* **2012**, *532*, 245−248.
(43) Van Swygenhoven, H.; Caro, A. Plastic Behavior of Nanophase Metals Studied by Molecular Dynamics. *Phys. Rev. B: Condens. Matter Mater. Phys.* **1998**, *58*, 11246−11251.
(44) Pinkert, S.; Grozic, J. L. Failure Mechanisms in Cemented Hydrate-Bearing Sands. *J. Chem. Eng. Data* **2015**, *60*, 376−382.
(45) Yoneda, J.; Kida, M.; Konno, Y.; Jin, Y.; Morita, S.; Tenma, N. In Situ Mechanical Properties of Shallow Gas Hydrate Deposits in the Deep Seabed. *Geophys. Res. Lett.* **2019**, *46*, 14459−14468.
(46) Wu, J.; Skallerud, B.; He, J.; Zhang, Z. Grain-size Induced Strengthening and Weakening of Dislocation-free Polycrystalline Gas Hydrates. *Procedia IUTAM* **2017**, *21*, 11−16.
(47) Ryou, H.; Drazin, J. W.; Wahl, K. J.; Qadri, S. B.; Gorzkowski, E. P.; Feigelson, B. N.; Wollmershauser, J. A. Below the Hall−Petch Limit in Nanocrystalline Ceramics. *ACS Nano* **2018**, *12*, 3083−3094.
(48) Craw, L.; Qi, C.; Prior, D. J.; Goldsby, D. L.; Kim, D. Mechanics and Microstructure of Deformed Natural Anisotropic Ice. *J. Struct. Geol.* **2018**, *115*, 152−166.

https://doi.org/10.1021/acs.jpcc.1c00901
J. Phys. Chem. C 2021, 125, 10034−10042